Supporting Information

Photoacoustic imaging of lithium metal batteries

Huihui Liu,[1,‡] Yibo Zhao,[1,‡] Jiasheng Zhou,[1] Ping Li,[1] Shou-Hang Bo,[*,1] and Sung-Liang Chen[*,1,2]

[1]University of Michigan-Shanghai Jiao Tong University Joint Institute, Shanghai Jiao Tong University, Shanghai 200240, China

[2]State Key Laboratory of Advanced Optical Communication Systems and Networks, Shanghai Jiao Tong University, Shanghai 200240, China

*E-mails: shouhang.bo@sjtu.edu.cn (S.H.Bo); sungliang.chen@sjtu.edu.cn (S.L.Chen)

‡These authors contribute equally to this work.

1. Sample preparation of the Li/Li cell

In this study, a Li/Li liquid electrolyte symmetric cell, consisting of two Li metal electrodes and a liquid electrolyte layer (Figure S1a), was used to showcase PAM imaging of Li protrusions. The liquid electrolyte layer was fabricated using a GFS (GF/D, Whatman) soaked in 1 M LiPF$_6$ electrolyte solution with 1:1:1 (volumetric ratio) ethylene carbonate (EC): diethyl carbonate (DEC): dimethyl carbonate (DMC) as a solvent. The thickness of the Li electrode was ~240 μm, and that of the GFS was ~2 mm before soaked and <2 mm after soaked. The diameter of the two Li electrodes was ~1.3 cm, and that of the GFS was ~1.5 cm. To facilitate PAM imaging, a flat cross-sectional sidewall surface was prepared by cutting the Li/Li cell through its sandwich stack, as shown in Figure S1b. Note that the imaged Li electrode thickness varied from <50 μm to up to ~300 μm (as described in the main text), which was different from the original thickness of the Li electrode (~240 μm, before cutting the Li/Li cell sample (Figure S1a)). This is most likely a result of mechanical damage to Li metal during cutting the Li/Li cell sample (Figure S1b). One corner of the Li electrode was further removed to mark the location for imaging. For the electrochemistry test, the Li/Li cell was first sealed in a stainless steel coin cell case (CR2016, Shenzhen Teensky Technology, Shenzhen, China), as shown in Figure S1c, before the galvanostatic (i.e., constant current) charging process of the Li/Li cell. After charging, the Li/Li cell was removed from the stainless steel coin cell. Figure S1d illustrates the Li/Li cell before and after charging. The direction of the current determines which of the electrodes that Li is stripped from or is plated onto, as shown in Figure S1d. In general, more protrusions will be formed for charging at high areal capacity. In this study, several Li/Li cells were charged at different current densities of 0.1, 0.2, 0.3, 0.5, and 1 mA/cm^2, respectively, because current density was considered as a major factor affecting the morphology of deposited Li. For each

charging current density, the charging time was fixed at 15 hours, and thus, higher current density resulted in larger amount of Li metal deposition (or stripping), which was also confirmed by PAM imaging (as described in the main text). Figure S1e shows Li/Li cell voltages as a function of elapsed time at five different charging current densities. For each charging current density, a representative voltage curve from one Li/Li cell sample was plotted. Before PAM imaging, the Li/Li cell, either with or without the charging process, was sealed in a plastic bag filled with liquid (EC:DMC or silicon oil), which was used to facilitate ultrasound coupling without chemically reacting with or physically dissolving any component of the Li/Li cell.
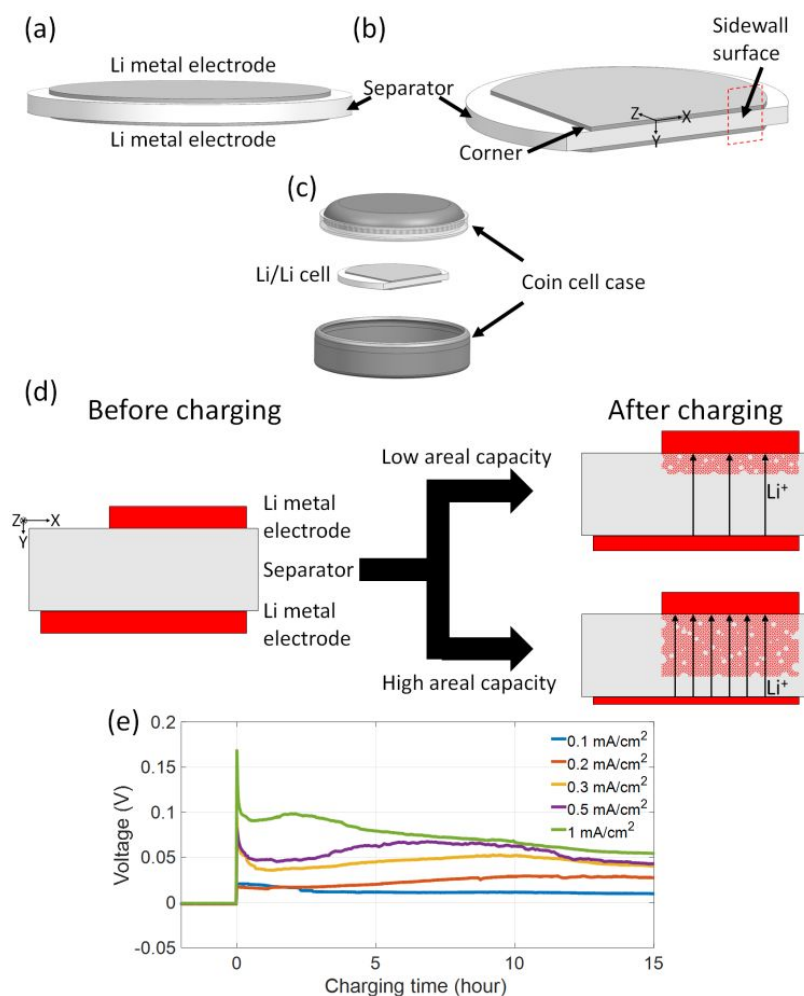

Figure S1. (a) Schematic of a Li/Li liquid electrolyte symmetric cell. (b) Schematic of the flat cross-sectional sidewall surface of the Li/Li cell with one corner of the Li metal removed as a

marker. (c) Schematic of the Li/Li cell sealed in a stainless steel coin cell case. (d) Illustration of the Li/Li cell before and after charging. Current is along the −Y (upward) direction for charging. More protrusions will be formed for charging at high areal capacity. (e) Cell voltages as a function of elapsed time at different charging current densities.

2. PAM imaging system

The schematic of the PAM system is shown in Figure S2a. A 532 nm pulsed laser (FDSS532-Q4, CryLaS, Germany) was used for photoacoustic imaging. The laser pulse duration was <2 ns, and the repetition rate was 1 kHz. The laser emitted from the laser head was split into two beams by using a beamsplitter (BS025, Thorlabs). The 10% reflected power was detected by a photodiode (DET10A2, Thorlabs) and was used as trigger signals. The 90% transmitted power was attenuated, spatially filtered, and focused by an objective lens (AC254-030, Thorlabs), which was used to excite photoacoustic signals. To facilitate PAM imaging of the cross-sectional sidewall surface of the Li/Li cell, a sample holder was custom made, as shown in Figure S2b. By using the sample holder, the Li/Li cell can be stably fixed with its sidewall surface facing upward. A water tank was also custom made, and it was used to facilitate ultrasound coupling. Both the sample holder and the water tank were mounted on a 3D linear motorized stage (M-404, Physik Instrumente [PI], Karlsruhe, Germany), as shown in Figure S2a, for scanning during image acquisition. As for detection of photoacoustic waves, a custom-made needle hydrophone (central frequency: 35 MHz) was employed and placed obliquely to the optical axis. Then, the photoacoustic signals were amplified by a preamplifier (ZFL-500LN-BNC+, Mini-Circuits, New York) and sampled by a digitizer (CSE1422, GaGe, Illinois) with sampling rate of 200 MS/s and 14-bit resolution. The data recorded by the digitizer were transferred to a computer for post signal processing and image formation. For post signal processing, a matched filter of 20–60

MHz was adopted to enhance signal-to-noise ratios (SNRs). Note that in this work, the laser energy used was ~86 nJ (per pulse) and no signal averaging was applied unless otherwise specified. The laser energy of ~86 nJ was chosen because it was below the damage threshold of the Li/Li cell used in this work based on our calibration results, as described later in Figure S3.
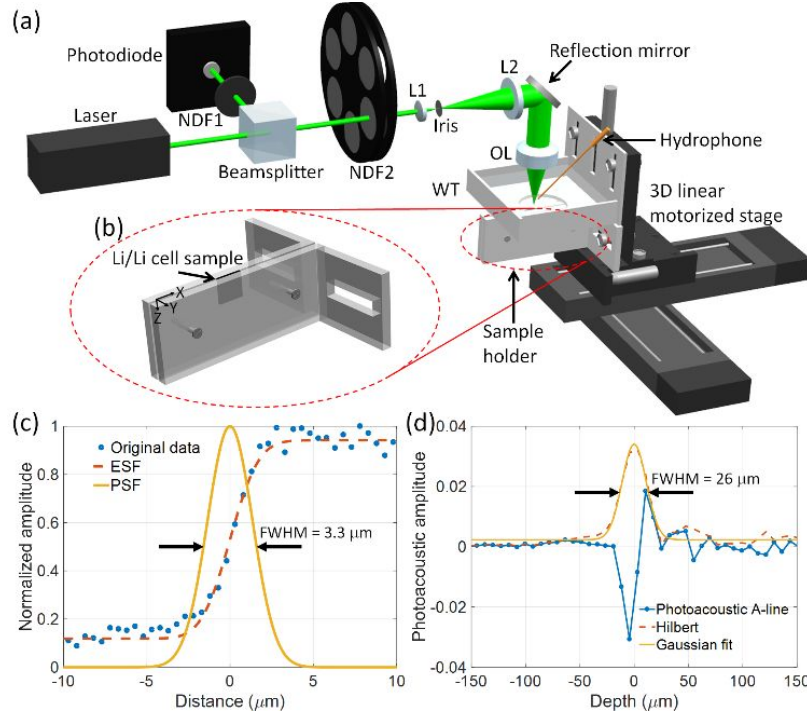
Figure S2. (a) Schematic of the PAM system. (b) Custom-made sample holder. (c) Calibration of lateral resolution. (d) Measurement of axial resolution. NDF1, neutral density filter 1; NDF2, neutral density filter 2; L1, lens 1; L2, lens 2; OL, objective lens; WT, water tank; PSF, point spread function.

The sharp edge of a razor blade was imaged to calibrate lateral resolution of our PAM system. Figure S2c shows the lateral profile of photoacoustic signals with scanning step size of 0.5 μm. The profile was fitted by an edge spread function (ESF). Then, we took the first derivative of the ESF to obtain a line spread function and extracted its full width at half maximum (FWHM) as lateral resolution, which was 3.3 μm. Note that higher lateral resolution of PAM can be realized

by using a lens with a higher NA for light focusing. As for measuring axial resolution, a 6-µm-diameter carbon fiber was imaged. Figure S2d shows the photoacoustic A-line signal from the carbon fiber and its Hilbert transform (envelope detection). The axial resolution was determined to be 26 µm from the FWHM of the envelope.

3. Calibrations of damage threshold and penetration depth

To calibrate the damage threshold of the Li metal of the Li/Li cell under the illumination of 532 nm pulsed laser, several Li foil pieces were imaged by PAM under different laser energy. Since both EC:DMC and silicon oil were used as acoustic coupling media in this work, both liquids were used in this calibration. Four Li metal foil samples sealed in plastic bags were prepared inside an Argon-filled glove box. EC:DMC was used as acoustic coupling media for two samples, and silicon oil for the other two samples. The former two were to be illuminated under laser energy of ~86 nJ and ~185 nJ (per pulse), respectively, and so do the latter two. We first took OM images of the corner of the four Li metal foil samples (the first column in Figure S3). Then, a small region around the corner of the four samples was imaged by PAM (the dashed boxes in the third column in Figure S3). After PAM acquisition, OM images of the same corner of the four samples were taken (the second column in Figure S3). As can be seen in Figures S3b and S3e under laser energy of ~86 nJ, OM images after PAM acquisition do not exhibit obvious differences between the PAM regions (referring to the dashed boxes in Figures S3c and S3f, respectively) and the rest. By contrast, in Figures S3h and S3k under laser energy of ~185 nJ, discernible darkened regions corresponding to the PAM regions (referring to the dashed boxes in

respectively) for the OM images after PAM acquisition can be clearly identified. The darkened regions were a result of the high-energy pulsed laser which caused the Li metal foil to fall off, thus losing metallic luster. Hence, the damage threshold was determined to be between ~86−185 nJ for the two coupling media, silicon oil and EC:DMC. The laser energy of ~86 nJ was used in this work, as mentioned previously. Note that in Figure S3, by comparing the OM images before and after PAM image acquisition, the latter also shows darkened color randomly, even in the regions without taking PAM. This may be due to the oxidation of Li metal itself during the time elapsed in the experimental process.
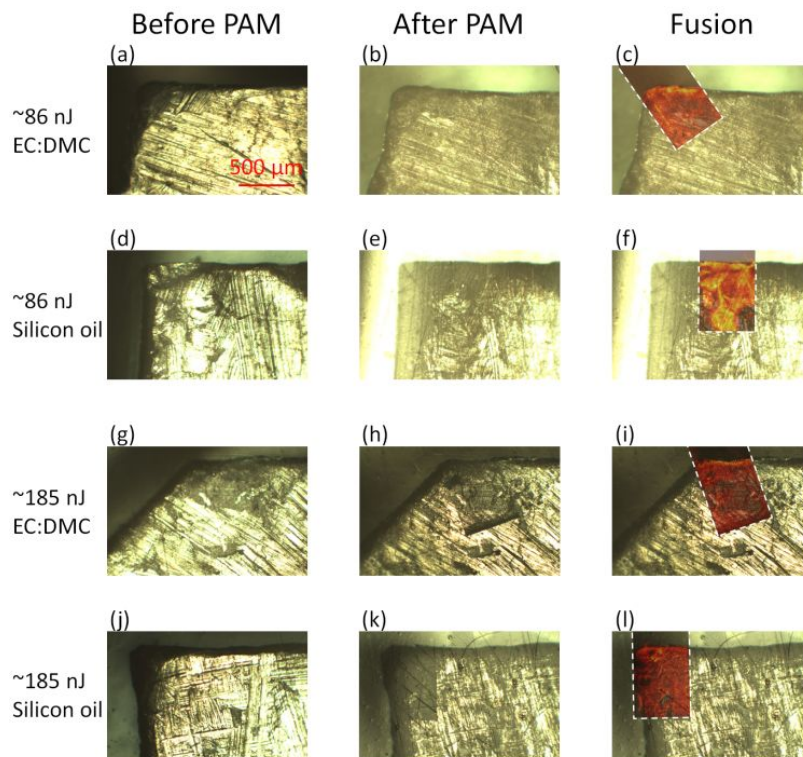
Figure S3. OM images before and after PAM acquisition under different laser energy and different acoustic coupling media. (a,b,c) Under laser energy of ~86 nJ with EC:DMC as the acoustic coupling medium. (d,e,f) Under laser energy of ~86 nJ with silicon oil as the acoustic coupling medium. (g,h,i) Under laser energy of ~185 nJ with EC:DMC as the acoustic coupling medium. (j,k,l) Under laser energy of ~185 nJ with silicon oil as the acoustic coupling medium. The first column shows the OM images before PAM acquisition, the second column shows the OM images after PAM acquisition, and the third column shows the fusion image of the PAM

image (the dashed boxes) and the OM image after PAM acquisition (the second column). All images share the same scale bar.

To measure the penetration depth of PAM for imaging Li inside the GFS of a Li/Li cell, we devised a sample consisting of three 51-µm-diameter tungsten wires (TWs). Note that the TW (instead of Li) was imaged because of the difficulty in preparing a sample with Li continuously distributed along the depth direction inside the GFS, and because of the similarity in the photoacoustic signal amplitudes from the TW and Li (described later). The measurement is detailed as follows: (1) Sample preparation for the calibration of penetration depth. (2) Measurement results of penetration depth. (3) Measurement of photoacoustic signal amplitudes from the TW and Li.

Sample preparation for the calibration of penetration depth. Figure S4a shows the schematic of the sample. First, a large piece of a PET film (~5 cm × 5 cm) was cut, polished by sandpaper, and cleaned by ethanol. It was used as the bottom holder. Then, a piece of the GFS (~1 cm × 1 cm) was prepared. The first TW (TW1) was obliquely inserted into the GFS. Note that the angle between the inserted TW1 and the surface of the GFS was kept small so that the surface of the GFS at the insertion position of TW1 will not be distorted too much. The two ends of TW1 were fixed on the bottom PET film by waterproof tapes. Then, the second TW (TW2) was placed above the GFS. As shown in Figure S4a, TW1 and TW2 are approximately in parallel along the X direction. Similarly, the two ends of TW2 were fixed on the bottom PET film by waterproof tapes. Another small piece of a PET film (~1 cm × 1 cm) was cut, polished, and cleaned, as mentioned above. As the top cover, the small PET film was placed over the GFS with TW1 and TW2 in between. The top PET film was pressed downward to make sure close contact of TW2

and the surface of the GFS, and then fixed with the bottom PET film by waterproof tapes. The third TW (TW3) was then placed above the top PET film and fixed by waterproof tapes. Next, a plastic film was used to cover the stack. Three sides of the plastic film were sealed with the bottom PET film by waterproof tapes. Before fully sealing the plastic film, the sample was put inside a glove box. The GFS was filled with EC:DEC:DMC, and then the sample was filled with liquid (EC:DMC) to facilitate ultrasound coupling. Finally, the last side of the plastic film was sealed by waterproof tapes inside the glove box.
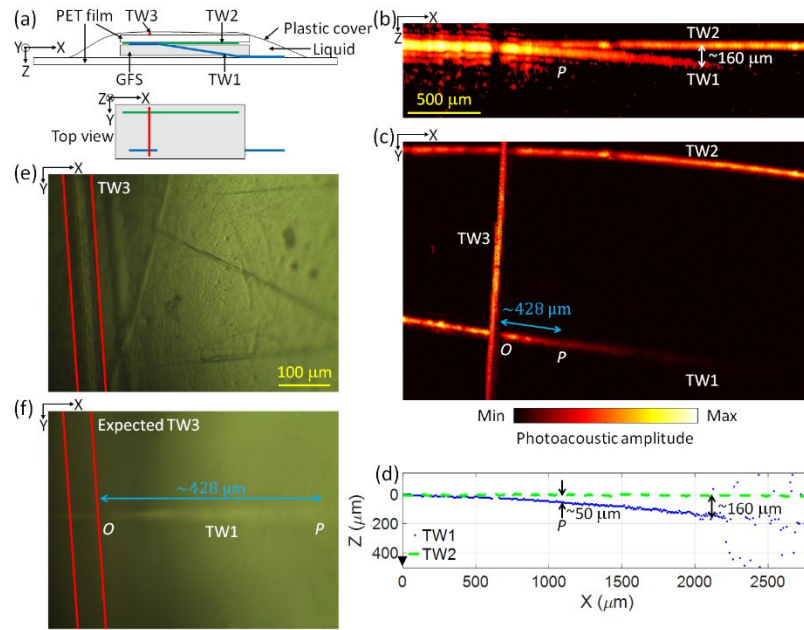

Figure S4. Calibration of penetration depth. (a) Schematic of the sample consisting of three TWs in side view (upper) and top view (lower). For better illustration, TW1 is plotted in blue, TW2 in green, and TW3 in red. (b,c) PAM MAP images of the sample in the XZ (b) and XY (c) planes. (b) and (c) share the same scale bar in (b). (d) Depth positions of maximum photoacoustic A-line signal amplitudes along the X direction. (e,f) OM images of the sample at the foci of TW3 (e) and TW1 (f). Red lines indicate the positions of TW3 and expected TW3. (e) and (f) share the same scale bar in (e).

Measurement results of penetration depth. Note that TW1 was obliquely inserted into the GFS for measurement of penetration depth of PAM. TW2 was placed right above the surface of

the GFS, which can be used as a reference of the surface of the GFS. TW3 was placed above a PET film with thickness of ~150 μm, which was used as a marker for estimation of penetration depth of OM. The PET film was used to ensure the flatness of the top surface of the GFS. The laser energy of ~86 nJ was used and signal averaging of 16 measurements was applied. Figures S4(b) and S4(c) show the PAM MAP images of the sample in the XZ and XY planes, respectively. We also checked the depth positions of maximum photoacoustic A-line signal amplitudes along the X direction, as shown in Figure S4(d). From Figure S4b and S4d, the penetration depth inside the GFS by PAM was measured to be ~160 μm. Penetration depth can be further enhanced by boosting SNRs, such as using an acoustic detector with higher sensitivity and/or applying more signal averaging. On the other hand, Figures S4e and S4f show the OM images of the sample at the foci of TW3 and TW1, respectively. As mentioned above, TW3 was used as a marker. Specifically, we took the OM image of TW3 first, and then took that of TW1 by adjusting the focus of the objective while the lateral position of the sample was kept the same. In this way, we were able to infer the position of TW3 in Figure S4f because Figures S4e and S4f are considered to be co-registered in the lateral direction. In Figure S4f, the intersection of TW1 and TW3 is denoted as O, and the position where TW1 becomes invisible is denoted as P. Then, the distance OP of ~428 μm can be obtained. Next, by comparing Figure S4f with Figure S4c, the corresponding positions O and P in Figure S4c can be determined. Further, by comparing Figures S4c with Figures S4b and S4d, the corresponding position P in Figures S4b and S4d can also be labeled, and the depth of TW1 at P can be obtained. Finally, the penetration depth inside the GFS by OM was determined to be ~50 μm, which was much shallower than PAM. The results suggest that PAM allows much deeper penetration with high contrast inside the GFS compared with OM, and thus holds promise for 3D visualization of Li inside the GFS. The laser

energy above the damage threshold can be used under certain circumstances, for example, only one-time imaging needed. Therefore, we also calibrated the penetration depth by using higher laser energy of ~185 nJ and ~357 nJ. Similarly, signal averaging of 16 measurements was applied. Figures S5a and S5b show the PAM MAP (XZ) images of the sample and corresponding depth positions of maximum photoacoustic A-line signal amplitudes along the X direction at laser energy of ~185 nJ and 357 nJ, respectively. The penetration depth can be deeper than ~220 μm. Interestingly, strong noise was observed with relatively strong photoacoustic signals (left regions in PAM MAP images in Figure S5), which could be due to the too high laser energy used. The exact reason is under investigation.
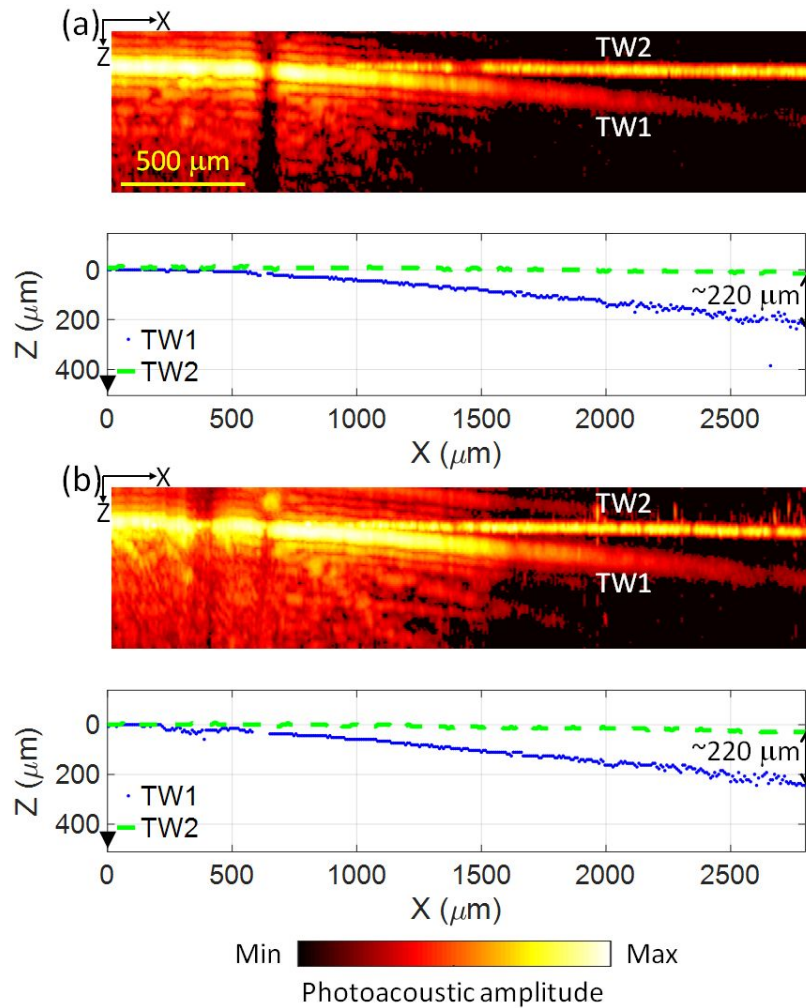
Figure S5. PAM MAP (XZ) images of the sample consisting of TWs and corresponding depth positions of maximum photoacoustic A-line signal amplitudes along the X direction at laser energy of ~185 nJ (a) and ~357 nJ (b). (a) and (b) share the same scale bar in (a).

Measurement of photoacoustic signal amplitudes from the TW and Li. In Figure S4, as mentioned previously, the TW (instead of Li) was imaged because of the difficulty in preparing a sample with Li continuously distributed along the depth direction inside the GFS. Since Li was expected to be imaged in practical applications for imaging of Li metal batteries, we here compared the photoacoustic signal amplitudes from the TW and Li. Note that in Figure S4, the photoacoustic signal of TW1 was measured when it was placed below a PET film with thickness of ~150 μm. Thus, we used the same arrangement (i.e., TW below a PET film) for fair comparison. On the other hand, the photoacoustic signal of Li was measured without a PET film above Li, as are the cases in our demonstrations in the main text. The laser energy used was ~86 nJ. EC:DMC was used for ultrasound coupling. Figures S6a and S6b show the PAM MAP (lateral) images of the TW below a PET film and Li, respectively, and Figure S6(c) shows the top 100 photoacoustic signal amplitudes of them. As can be seen, approximately the photoacoustic signal amplitudes of the TW and Li were similar. The ratio of the average of the top 100 photoacoustic signal amplitudes from the TW to that from Li was also calculated, which was 87%. Since the photoacoustic signal amplitudes from the TW and Li were measured to be similar, the alternative approach to calibrating the penetration depth of PAM was considered to be reasonable. That is, the penetration depth of ~160 μm for Li inside the GFS can be anticipated.
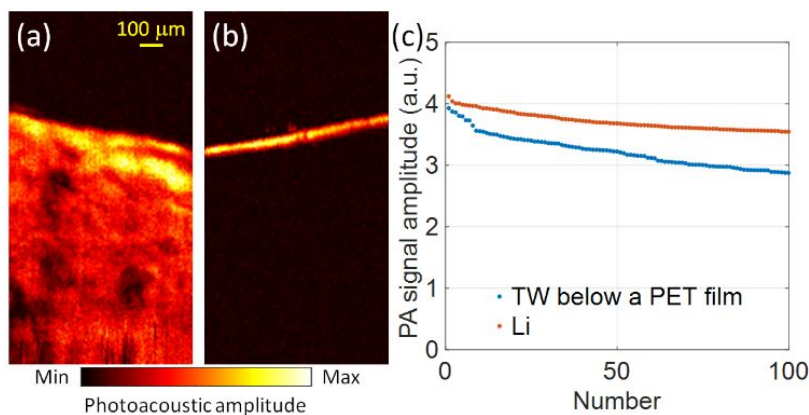
Figure S6. (a,b) PAM MAP (lateral) images of the TW below a PET film (a) and Li (b). (c) The top 100 photoacoustic signal amplitudes of the TW below a PET film and Li. (a) and (b) share the same scale bar in (a).

4. Calculation method of the Li ratio and error range

An intensity threshold was estimated by graythresh function in Matlab using the acquired PAM MAP image (denoted as aPAM). Then, the intensity threshold was used to obtain a binarized image, i.e., pixels corresponding to either Li or background. Using the binarized image, the Li ratio (i.e., blue squares in Figure 3c) can be calculated as the number of pixels with Li over the total number of pixels. As for the error range of the Li ratio (i.e., error bars in Figure 3c), the same procedure was used to calculate the upper- and lower-bound Li ratios with two different intensity thresholds. Similarly, by Matlab graythresh function, the intensity threshold for upper-bound Li ratio calculation was obtained from the image with noise subtracted from aPAM (i.e., aPAM − noise), while that for lower-bound Li ratio calculation from the image with noise added to aPAM (i.e., aPAM + noise).